

Article

The Optical Properties of Host Galaxies of Radio Sources in the Coma Cluster

Xiaolan Hou ¹, Heng Yu ^{1,*}, Tong Pan ², Hu Zou ^{3,4}, Haoran Dou ¹, Emily Moravec ⁵ and Chengkui Li ⁶

- ¹ School of Physics and Astronomy, Beijing Normal University, Beijing 100875, China; houxl@mail.bnu.edu.cn (X.H.); 202321160002@mail.bnu.edu.cn (H.D.)
- ² Leiden Observatory, Leiden University, Einsteinweg 55, 2333 CC Leiden, The Netherlands; tpan@strw.leidenuniv.nl
- ³ National Astronomical Observatories, Chinese Academy of Sciences, Beijing 100101, China; zouhu@nao.cas.cn
- ⁴ School of Astronomy and Space Science, University of Chinese Academy of Sciences, Beijing 101408, China
- ⁵ Green Bank Observatory, P.O. Box 2, Green Bank, WV 24944, USA; emoravec@nrao.edu
- ⁶ Key Laboratory of Particle Astrophysics, Institute of High Energy Physics, Chinese Academy of Sciences, Beijing 100049, China; lick@ihep.ac.cn
- * Correspondence: yuheng@bnu.edu.cn

Abstract

We present a comprehensive study of host galaxies of radio sources within the $1.35R_{200}$ of the Coma cluster by combining deep 144 MHz observations from the LOFAR Two-Metre Sky Survey (LoTSS-DR2) with optical spectroscopy and photometry from DESI and SDSS. We identify 79 spectroscopically confirmed cluster members with reliable radio emission and classify them into compact, extended, and tailed subsamples according to their radio morphologies. By combining their radio and optical properties, we find compact radio sources are predominantly associated with massive, quiescent galaxies driven by AGN activity, while tailed sources are largely hosted by star-forming galaxies, tracing ongoing ram pressure stripping (RPS). Using phase-space analysis and a projected infall time proxy (d_R), we find that extended sources are preferentially located in the cluster outskirts ($d_R > 1$), while tailed sources are concentrated in the intermediate infall region ($0.4 < d_R < 1.0$), highlighting the influence of the dense intracluster medium.

Keywords: radio sources; coma cluster; galaxy evolution; ram pressure stripping; star-forming galaxies

1. Introduction

Galaxy clusters provide a powerful laboratory for studying how dense environments influence galaxy evolution. As the largest gravitationally bound systems in the Universe, clusters host a range of environmental mechanisms, such as ram pressure stripping, tidal interactions (including galaxy harassment), and starvation. These mechanisms act to remove, heat, or redistribute the cold gas that fuels star formation. Consequently, these processes can substantially alter the star formation rates (SFRs), optical colors, and morphological structures of galaxies, contributing to the well-established transformation from blue, star-forming spirals to red, quiescent early-type systems (e.g., [1,2]). Understanding how these mechanisms operate across different galaxy populations is central to disentangling the environmental drivers of galaxy evolution.

Radio continuum observations offer a complementary and uniquely sensitive probe of these evolutionary processes. Radio emission in galaxies primarily traces synchrotron

arXiv:2602.19050v1 [astro-ph.GA] 22 Feb 2026



Academic Editor: Firstname Lastname

Received: 22 December 2025

Revised: 6 February 2026

Accepted: 14 February 2026

Published:

Copyright: © 2026 by the authors.

Licensee MDPI, Basel, Switzerland.

This article is an open access article

distributed under the terms and

conditions of the [Creative Commons](#)[Attribution \(CC BY\) license](#).

radiation from relativistic electrons in magnetic fields, which are powered either by recent star formation (via cosmic rays from supernovae) or by active galactic nuclei (AGN) that launch jets and lobes (e.g., [3–6]). Since radio emission is not affected by dust obscuration, it reveals activity that may otherwise remain hidden in optical surveys. Furthermore, the diverse radio morphologies, including compact cores, extended jets, head-tail structures, and diffuse disk emission, encode critical information about both internal energy sources and the interaction between the interstellar medium (ISM) of a galaxy and the intracluster medium (ICM). Recent studies utilizing LOFAR data have explicitly demonstrated that the dynamic environment of merging clusters significantly impacts these morphologies, leading to a higher population proportion of disturbed and bent sources compared to relaxed clusters [7]. This makes radio data particularly valuable for characterizing environmental processing.

The optical properties of radio-hosting galaxies in clusters provide additional insight into these mechanisms (e.g., [8–10]). Massive early-type galaxies typically exhibit red colors and low star formation rates, with their radio emission predominantly powered by AGN activity (e.g., [11,12]). In contrast, lower-mass or morphologically disturbed galaxies often display bluer colors, where radio emission is linked to ongoing or recently triggered star formation. In these systems, the star formation activity is sometimes enhanced or spatially reshaped by ram-pressure interactions (e.g., [13,14]). Thus, the combination of radio and optical diagnostics enables a more holistic view of the interplay between star formation, AGN activity, and environmental transformation.

The Coma Cluster (Abell 1656) is one of the nearest and richest galaxy clusters ($z \approx 0.023$), with characteristic radii of $R_{500} \sim 1.3$ Mpc ($\approx 47'$) and $R_{200} \sim 2$ Mpc ($\approx 70'$) [15]. R_{500} and R_{200} are defined as the radii within which the average cluster density is 500 and 200 times the critical density of the Universe at the cluster's redshift, respectively. Due to its proximity and richness, Coma serves as an ideal laboratory for investigating the impact of dense environments on galaxy evolution and has been extensively observed across multiple wavelengths. It possesses deep optical photometric and spectroscopic coverage [16,17], full-field low-frequency radio imaging from LOFAR, and the latest X-ray measurements from the extended ROentgen Survey with an Imaging Telescope Array [eROSITA]; [18]. Together, these datasets provide a uniquely comprehensive, multi-band view of the cluster, enabling detailed studies of how the cluster environment shapes the properties and evolution of its member galaxies.

Previous high-frequency radio observations with the VLA have already revealed the diverse nature of radio emission in Coma. Using deep 1.4 GHz imaging, Miller et al. [19] detected over 600 radio sources across two $30' \times 50'$ fields targeting the cluster core ($\sim 0.4R_{200}$) and the southwest infall region ($\sim 1.25R_{200}$), identifying 38 as confirmed cluster members. These observations demonstrated that massive elliptical galaxies typically host AGN-powered emission, whereas fainter blue galaxies exhibit star formation-driven radio activity. More recently, Lal et al. [20] utilized the upgraded Giant Metrewave Radio Telescope (uGMRT) to provide a broader census of the cluster at 250–850 MHz across 4 deg^2 fields, characterizing the radio properties of 24 members and highlighting the presence of asymmetric or tail-like radio morphologies. Such features are consistent with ram-pressure interactions with the ICM during galaxy infall. These findings have established Coma as a benchmark system for studying environmental influences on galaxy activity through radio observations.

Compared to high/mid-frequency surveys, low-frequency observations at 144 MHz are significantly more sensitive to steep-spectrum and aged synchrotron emission. Such emission is expected to be prevalent in cluster galaxies undergoing environmental processes such as ram-pressure stripping. The excellent surface-brightness sensitivity of the LOFAR

Two-metre Sky Survey [LoTSS]; [21] therefore makes it particularly well suited for detecting extended radio tails and diffuse emission associated with environmental transformation, complementing earlier 1.4 GHz studies.

In this work, we combine deep LOFAR observations from the second data release of the LoTSS [LoTSS DR2]; [22] with optical imaging from the DESI Legacy Imaging Survey (DR9) and spectroscopic measurements from DESI DR1. We utilize these data to conduct a systematic analysis of the radio activity and optical properties of member galaxies extending from the cluster core out to the periphery. The primary goal of this study is to investigate the impact of the dense cluster environment on radio emission of galaxies across a wide range of local densities.

This paper is organized as follows. In Section 2, we describe the optical (DESI) and radio (LoTSS DR2) datasets, and outline the construction of the spectroscopically confirmed Coma galaxy sample alongside their LOFAR radio counterparts. Section 3 presents the physical properties of the host galaxies of radio sources in the cluster. In Section 4, we examine the environmental dependence of these radio populations using the $R - V$ diagram and the infall time proxy (d_R). Finally, Section 5 summarizes our main conclusions regarding the environmental modulation of radio activity in the Coma cluster.

2. Data and Samples

2.1. Optical Data

The optical photometric data used in this study are drawn from the DESI Legacy Imaging Survey (DR9; [16]), while the spectroscopic data are obtained from the DESI survey (DR1; [17]). We define a $4^\circ \times 4^\circ$ field ($\approx 6.72 \text{ Mpc} \times 6.72 \text{ Mpc}$ at $z = 0.023$) centered on NGC 4874 (R.A. = 194.90° , Decl. = 27.96°), the Brightest Cluster Galaxy (BCG) of the Coma cluster. This field of view covers both the cluster core and its extended outskirts.

From DESI DR1, we retrieved 22,360 galaxies with spectroscopic redshifts. Since the DESI target selection algorithm excludes very bright galaxies, we supplemented this dataset with spectroscopic measurements from the Sloan Digital Sky Survey (SDSS) [DR18] [23] to recover bright sources. The merged DESI+SDSS catalog contains 22,668 galaxies with reliable spectroscopic redshifts.

To assess the sample completeness, we selected 144,881 photometric sources with the r -band magnitude $mag_r < 22$ from the DESI Legacy Survey (DR9) within the defined field. The mag_r was derived from the measured flux according to the following relation: $mag_r = 22.5 - 2.5 \log_{10}(f_r/mw_trans)$. Here, the f_r is in units of nanomaggies and is corrected for the Galactic extinction using the mw_trans factor provided by the survey. Using this photometric catalog, we evaluated the spectroscopic completeness as shown in Figure 1. The DESI Bright Galaxy Survey (BGS) consists of a flux-limited BGS Bright sample ($mag_r < 19.5$) and a color-selected BGS Faint sample ($19.5 < mag_r < 20.175$) [24]. Consistent with this selection, we find that the spectroscopic completeness exceeds 92% for galaxies brighter than $mag_r = 19.5$, whereas it drops rapidly at fainter magnitudes. The spatial completeness of bright galaxies $mag_r < 19.5$ remains above $\sim 94\%$ within a radius of $1.35R_{200}$ ($94.5'$). Consequently, we defined a parent sample of 7957 galaxies with $mag_r < 19.5$ located within this central $1.35R_{200}$ circular region (covering an area of 7.8 deg^2) for cluster membership determination.

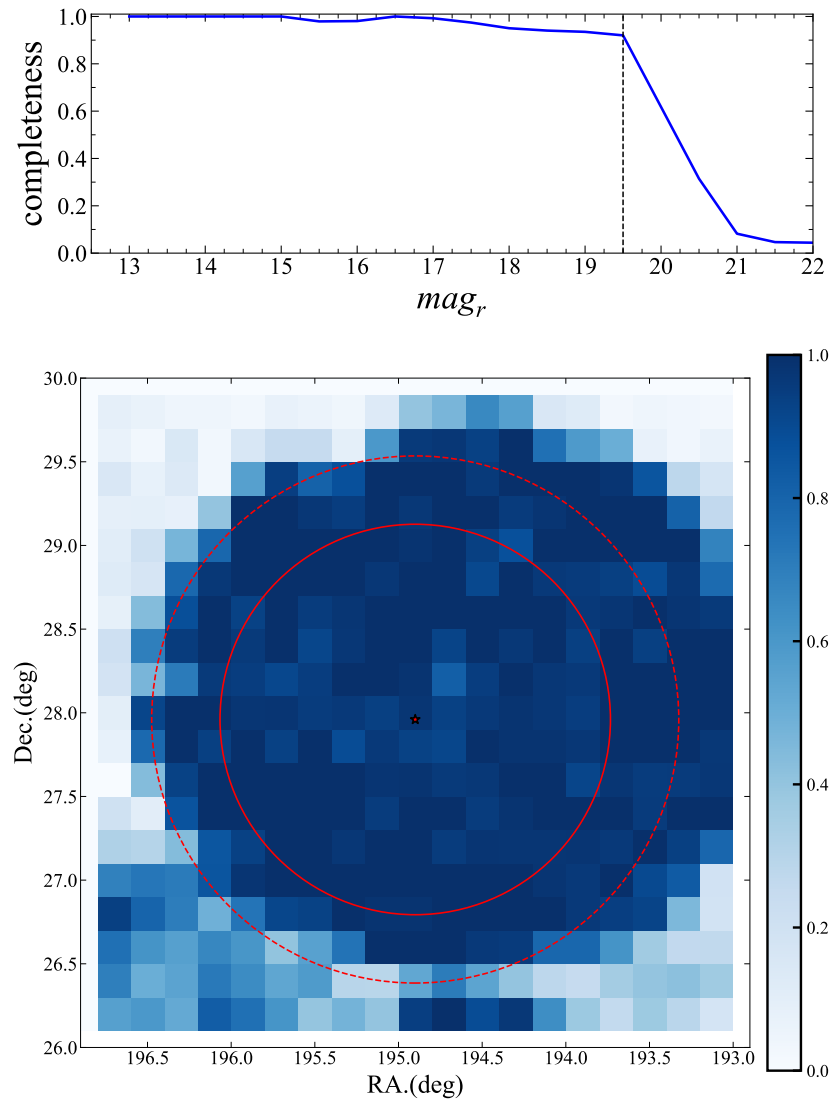


Figure 1. Spectroscopic data completeness. (**Upper panel**): Spectroscopic completeness as a function of r -band magnitude within $1.35R_{200}$. The vertical dashed line denotes $r = 19.5$ mag. (**Bottom panel**): Spatial distribution of the spectroscopic completeness. The colorbar represents the completeness at $r < 19.5$. The red solid circle indicates the radius of R_{200} , and red dashed circle indicates $1.35R_{200}$.

Cluster members were identified using the caustic technique [25,26]. This method identifies cluster members by determining the boundary of the galaxy distribution in the $R - V$ diagram, or the projected phase space (Figure 2), where R is the projected distance from the cluster center normalized with the R_{200} and V is the line-of-sight velocity relative to the cluster center. The boundaries, or ‘caustics’, represent the escape velocity profile of the cluster as a function of radius. Galaxies located within the caustic envelopes are considered gravitationally bound members. This method yields 1329 Coma members with a line-of-sight velocity dispersion (σ_{los}) of 818 km s^{-1} . Among these members, 1258 galaxies have stellar mass (M_*) and star formation rate (SFR) measurements available in the DESI Stellar Mass and Emission Line Catalog [27], where both quantities were derived via spectral energy distribution (SED) fitting using the CIGALE code [28].

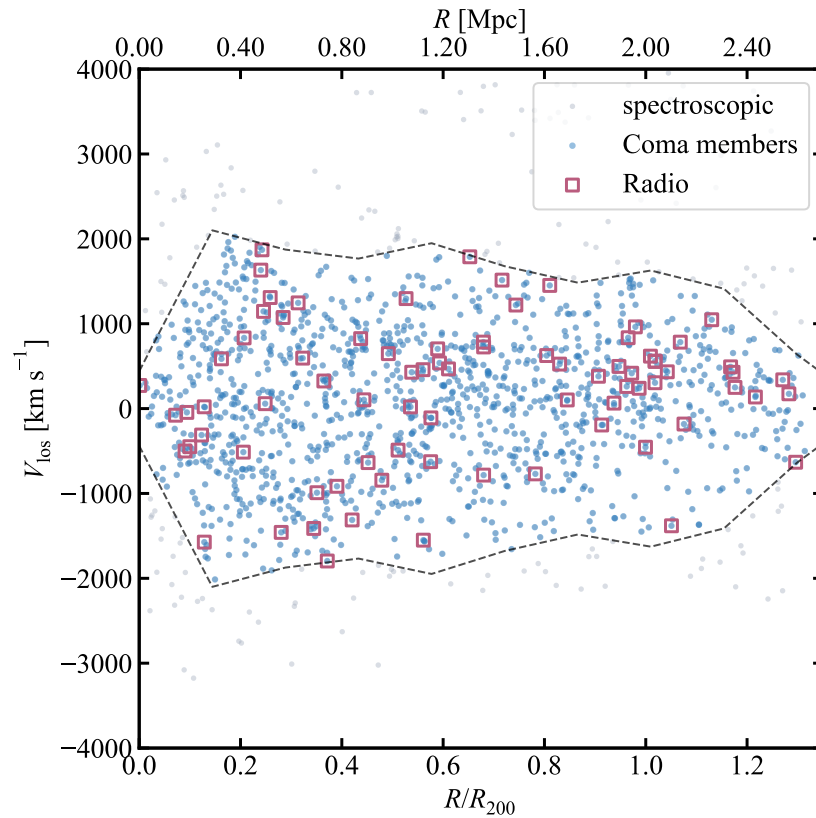


Figure 2. The $R - V$ diagram (R/R_{200} vs. V_{los}) of galaxies in the Coma Cluster field. Grey points represent spectroscopic galaxies with $r < 19.5$ mag. The black dashed curves indicate the caustic lines. Blue points denote confirmed Coma cluster members located within the caustic boundaries. The 79 galaxies with detected radio emission (LOFAR 144 MHz) are highlighted by red squares.

2.2. Radio Sources

The radio continuum data for this study are drawn from LoTSS-DR2 [22]. The survey was conducted at a central frequency of 144 MHz with a resolution of $6''$. The maps achieve a median RMS sensitivity of $83 \mu\text{Jy beam}^{-1}$ in Stokes I continuum. The astrometric accuracy is $0.2''$, and the flux density scale accuracy is approximately 10%. Based on peak brightness, the point-source completeness is estimated to be 90% at $0.8 \text{ mJy beam}^{-1}$. Within the same $4^\circ \times 4^\circ$ region utilized for the optical sample, a total of 11,287 radio sources were detected (Figure 3).

To assess the statistical properties and completeness of our radio sample, we derived the Euclidean-normalized differential source counts ($\log N - \log S$) for galaxies within $1.35R_{200}$ of the cluster center (Figure 4). The observed distribution generally aligns with the evolutionary models of Bonato et al. [29] and the empirical results from Galluzzi et al. [30]. Notably, a slight excess in the observed counts relative to the global models is apparent; this reflects the characteristic galaxy overdensity of the Coma cluster environment compared to the cosmic average.

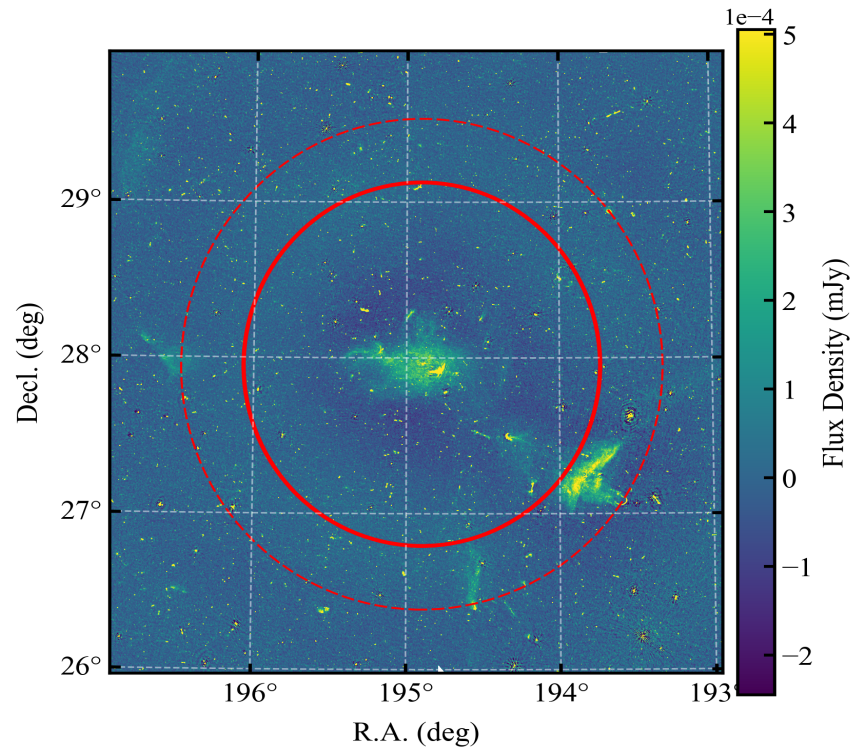


Figure 3. The LoTSS-DR2 radio continuum image of the Coma cluster region. This $4^\circ \times 4^\circ$ field is centered on NGC 4874, the brightest central galaxy of the cluster. Red circles are the same as Figure 1.

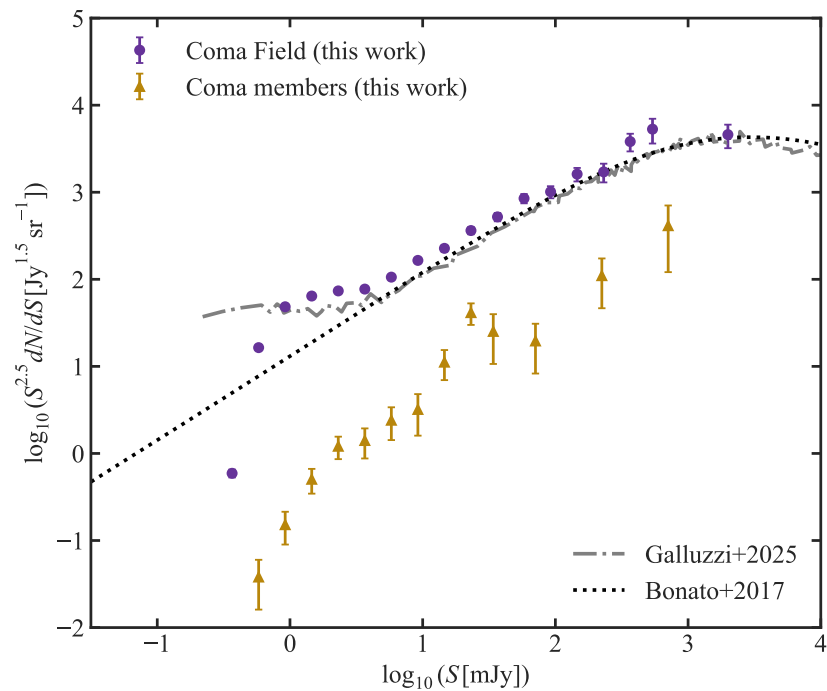


Figure 4. Euclidean-normalized differential source counts at 144 MHz within $1.35R_{200}$. Data points show the total counts in the Coma field (purple circles) and confirmed cluster members (golden triangles). Overlaid are models from Galluzzi et al. [30] (grey dash-dotted line) and Bonato et al. [29] (black dotted line), accounting for diverse extragalactic radio populations. Error bars indicate 1σ uncertainties.

To ensure the reliability of the radio detections, we established a threshold based on the Peak Signal-to-Noise Ratio (PNRs) calculated as the ratio of the peak flux density to the root-mean-square (RMS) noise within the source island, with RMS values adopted from

the LoTSS DR2 catalog. We selected radio sources with $\text{PNR} > 4$ for subsequent analysis, resulting in a final sample of 10,354 sources.

We proceeded to identify the counterparts of these radio sources that are spectroscopically confirmed Coma member galaxies using an initial search radius of $6''$. There are 72 radio sources that meet the criteria. Recognizing that irregular radio/optical morphologies may lead to inaccurate centroid identification, we performed an additional visual examination for sources exhibiting positional offsets between $6''$ and $20''$. There are 7 more members identified by the visual check. Their optical/radio images are shown in Appendix B. After this verification process, our final sample comprises 79 Coma cluster members with radio emission (see Figure 2).

We also compare our sample with 24 member sources reported by Lal et al. [20]. There are 14 members overlapping, 8 sources not recognized as members by the caustic method. NGC 4827 and NGC 4869 are visible in the LOFAR image, but not listed in the LoTSS DR2 catalog somehow. Thus they are not included in our sample. This would not affect the statistics of our sample.

Furthermore, the source counts for the confirmed Coma cluster members are highlighted as golden triangles in Figure 4. The distribution of these cluster members follows a similar trend to the total field counts, but their numbers are too few to fully account for the observed excess, which may be due to gravitational lensing that amplifies the brightness of background radio sources.

We classify these radio sources into three distinct types based on their radio morphology. Compact (C) sources are defined following the criteria in Rickel et al. [7], exhibiting roughly circular emission with an angular size smaller than $12''$ (approximately twice the LoTSS survey resolution). Extended (E) sources show clearly elongated or irregular emission features with angular sizes greater than $12''$. We also isolated sources with distinct Tailed (T) structures as a separate category, typically characterized by a swept-back emission strongly indicative of galactic motion or ram-pressure stripping (RPS) processes. Exemplary sources of each classification are shown in Figure 5. Based on the visual inspection and morphological criteria described above, our 79 radio sources are classified into 31 compact sources, 25 extended sources, and 23 tailed structures.

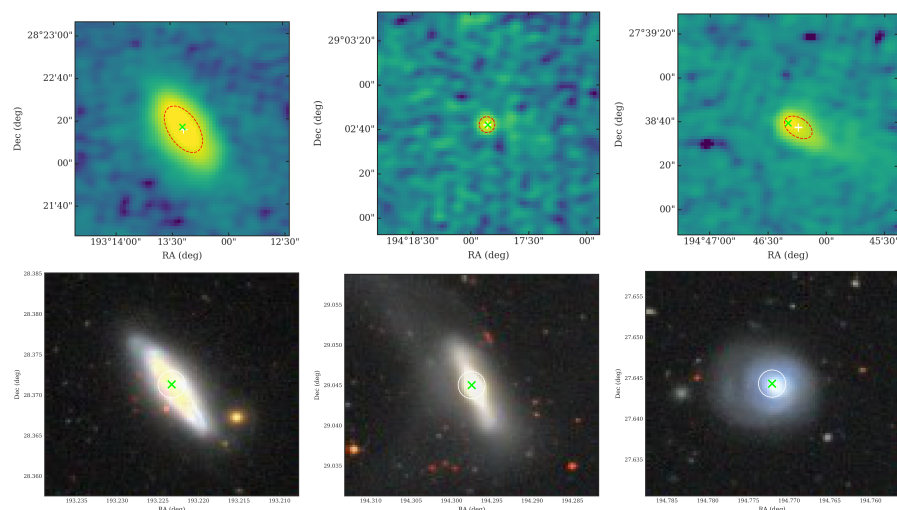


Figure 5. Examples of radio sources classified by morphology: extended (E), compact (C), and tailed (T). The (top panels) display the LOFAR 144 MHz radio continuum images, each covering a field of view of $100'' \times 100''$, while the (bottom panels) show the corresponding optical images from DESI. In all panels, green “x” symbols indicate the optical galactic centers, and white crosses denote the centroids of the radio emission. The red dashed ellipses in the radio images represent the morphology detections of the radio emission. The white circles in the optical images have a radius of $6''$.

We also examined the spatial distribution of these 79 member radio sources and marked the tail directions of the tailed sources (Figure 6). It can be seen that they are primarily concentrated along the northeast–southwest direction, which aligns with the merger direction of the infalling NGC 4839 group. Most tailed sources are located within R_{500} , where the ICM is quite dense. However, we have not identified a clear or physically meaningful pattern in these tail directions; they are largely randomly distributed.

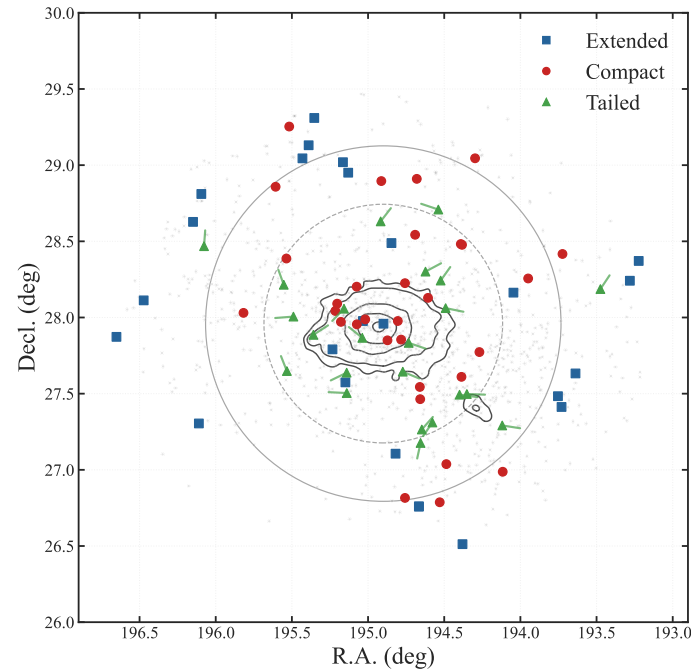


Figure 6. The spatial distribution of 79 member radio sources. The grey dots represent optical Coma members. Radio sources are color-coded by morphology: blue squares for extended (E), red circles for compact (C), and green triangles for tailed (T) structures. The tails of tailed sources are marked with short lines. The black contours show ROSAT X-ray surface brightness [31]. The solid grey circle represents the R_{200} , while the dashed circle represents R_{500} .

3. Optical Properties of Host Galaxies

3.1. Star-Forming and Quiescent Populations

To explore the optical properties of the host galaxies of radio sources in our sample, we adopt a specific star formation rate (sSFR) threshold of $\log(\text{sSFR}) = -11 \text{ yr}^{-1}$ [32] to distinguish between actively star-forming (SF) and quiescent (Q) systems. Based on this criterion, our sample comprises 34 star-forming galaxies and 45 quiescent galaxies. Figure 7 shows the distribution of these galaxies in the $\log(M_*)$ - $\log(\text{SFR})$ plane. Extended (E) sources are represented by blue squares, Compact (C) sources by red circles, and Tailed (T) structures by green triangles. Quiescent galaxies are indicated by filled markers, while star-forming galaxies are shown with open markers.

The host galaxies in our sample clearly exhibit a bimodal distribution, populating either the actively star-forming sequence ($\log \text{SFR} > -1$) or the region of high stellar mass ($\log M_* > 10.5 M_\odot$). A strong correlation is evident between radio morphology and optical state: the vast majority (25 out of 31) of compact sources are associated with quiescent galaxies, suggesting that their radio emission is primarily attributed to the central AGN activity, which is a typical characteristic of massive elliptical systems [33,34]. In contrast, a significant portion (16 out of 23) of the tailed structures originates from star-forming galaxies. Specifically, nine of these star-forming tailed sources have been previously confirmed as optical RPS galaxies by Chen et al. [35]. Although the RPS validation sample

from Chen et al. [35] only covers the central part of our field ($\sim 1.25 \text{ deg}^2$), this significant overlap indicates that the radio tails primarily originate from star formation within cool gas stripped by environmental processes, such as RPS or tidal interactions. Conversely, the radio tails observed in quiescent galaxies are more likely related to jets and outflows powered by their central AGN. The extended radio sources, however, show a near-equal division between star-forming galaxies (12) and quiescent galaxies (13). It is inherently difficult to morphologically disentangle whether the extended radio emission originates from star-forming regions (diffuse disk emission) or from AGN-driven jets/lobes in this class. However, the SFR measured in the optical band provides a crucial constraint to quantify the relative contribution from star formation activity. Future studies incorporating far-infrared (FIR) flux would be beneficial in providing a more robust, dust-independent census of star formation and enabling improved cross-calibration with radio-based indicators.

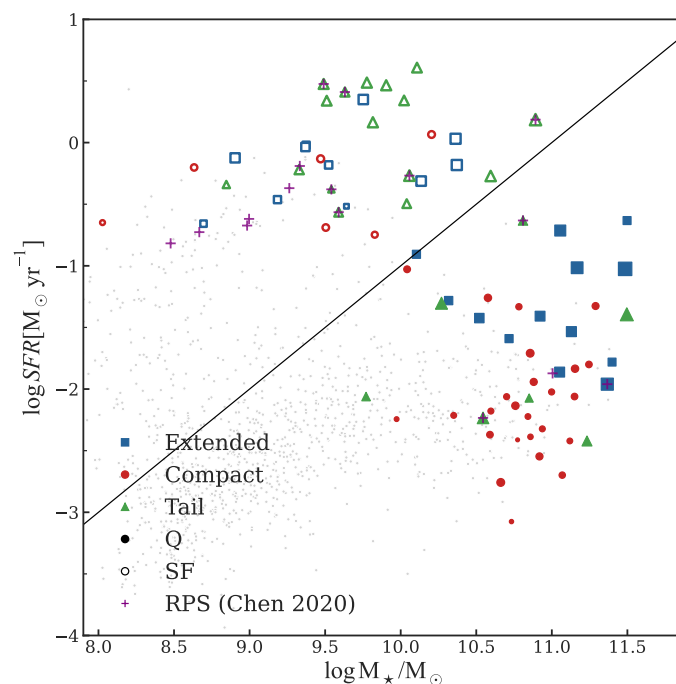


Figure 7. Distribution of galaxies in the $\log \text{SFR}-\log M_*$ plane. The grey dots represent optical Coma members. Radio sources are color-coded by morphology: blue squares for extended (E), red circles for compact (C), and green triangles for tailed (T) structures. The black solid line denotes a specific star formation rate of $\log \text{sSFR} = -11 \text{ yr}^{-1}$. Galaxies are further categorized based on this threshold: star-forming galaxies (SF) are shown as open symbols, while quiescent galaxies (Q) are shown as filled symbols. The size of markers reflects the radio luminosity at 144 MHz ($\log L_{144}$). The purple crosses represent optical RPS galaxies identified by Chen et al. [35].

3.2. AGN-Dominated Versus Star Formation-Dominated Activity

To further investigate whether the radio emission in these galaxies is dominated by AGN or star formation (SF), we examined the relationship between the 144 MHz radio luminosity (L_{144}) and the SFR of the galaxies. The L_{144} was calculated for each galaxy from the observed total integrated flux density (F_{tot}) reported in the LoTSS-DR2 catalog, following standard radio K-correction procedures. The luminosity was computed using the following cosmological relation [36]:

$$L_{144}[\text{W Hz}^{-1}] = 4\pi D_L^2[\text{m}^2] F_{\text{tot}}[\text{mJy}] 10^{-29} (1+z)^{\alpha-1} \quad (1)$$

Here, D_L is the luminosity distance in meters, F_{tot} is the observed total integrated flux density in mJy, and z is the spectroscopic redshift. Following conventional practice

for K-correction in this band, the radio spectral index α (defined as $S \propto \nu^{-\alpha}$) is fixed at a constant value of $\alpha = 0.7$ [37]. At low redshift, the choice of α has a minimal impact on the K-correction. For the Coma cluster ($z \approx 0.023$), varying α from 0.7 to 0.3 results in a change of only $\sim 1.6\%$ in the derived luminosity.

The distribution of L_{144} and \log SFR for Coma members is shown in Figure 8. It can be seen that compact sources (C) are relatively dim, clustering towards the lower left portion of the figure, consistent with low-power AGN activity. Radio sources exhibiting extended structures (E) or tailed structures (T) are more diverse, displaying a range of luminosities and SFRs. The $6''$ resolution of the LoTSS survey corresponds to a physical scale of 2.8 kpc at the distance of the Coma cluster. This resolution provides crucial visual insight into the origin of the radio emission. Extended radio emission originating purely from star-forming regions typically shows a good morphological correspondence with the galaxy's optical structure.

To quantitatively disentangle the AGN and SF contributions, we utilize an empirical radio-SFR relation derived from the LoTSS Deep Fields [38,39]:

$$\log_{10} L_{144} [\text{W Hz}^{-1}] = 22.06 + 1.07 \log_{10} \text{SFR}, \quad (2)$$

This relation, depicted by the black dashed line in Figure 8, Gürkan et al. [38], represents the expected radio luminosity contributed by star formation alone. Radio sources with measured luminosities exceeding this relation by more than a factor of three are considered to require an additional contribution from an AGN. We find that the star-forming galaxies (open markers) and quiescent galaxies (filled markers) maintain a distinct separation in this diagram. This observed separation is consistent with the expectations set by the radio-SFR relationship. Consequently, it is reasonable to conclude that the radio activity observed in quiescent galaxies is predominantly AGN-dominated, while in SF galaxies, a significant portion of their radio emission is contributed by ongoing star formation activity.

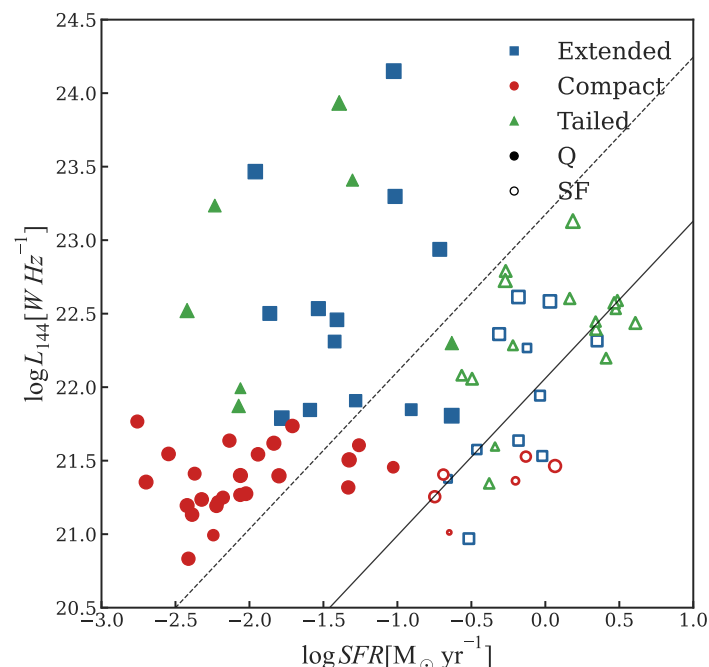


Figure 8. SFR versus the radio luminosity of radio sources within the Coma members. The black solid line represents the best-fit relation for star-forming galaxies derived by Gürkan et al. [38], and the black dashed line represents 3σ above this relation. Marker types and colors are the same as in Figure 7. The size of markers is scaled with stellar masses (M_*) of each galaxy.

3.3. The Color–Magnitude Relation

We examined the distribution of the host galaxies of radio sources on the Color–Magnitude Diagram (CMD), as depicted in Figure 9. To establish the baseline stellar population for comparison, we first determined the Color–Magnitude Relation (CMR), commonly referred to as the Red Sequence (RS). The RS was derived using an iterative σ -clipping least-squares fitting procedure, performed exclusively on the spectroscopically confirmed Coma cluster members. This technique effectively suppresses contamination from blue cloud galaxies and interlopers, accurately capturing the intrinsic scatter of the passive galaxy population [40]. At each iteration, a linear function of the form $\text{mag}_g - \text{mag}_r = f\text{mag}_r + fi$ was fitted to the data. Galaxies whose color residuals exceeded 3σ from the current best-fit relation were iteratively excluded, and the fitting process was repeated until the slope (α) and intercept (β) converged to within a relative change of 10^{-4} , or until a maximum of ten iterations was reached [41]. This procedure yielded a stable and robust characterization of the cluster RS. The final fitted RS is described by the linear relation: $\text{mag}_g - \text{mag}_r = -0.027\text{mag}_r + 1.158$.

Generally, the radio sources in our sample are distributed primarily along the bright end of the CMD. The AGN-dominated radio sources (filled markers in Figure 9), which are predominantly associated with quiescent galaxies identified via radio excess emission, are found to lie close to the red sequence. This observed behavior is consistent with the established picture in which radio-loud AGN preferentially reside in massive, quiescent early-type hosts whose cold gas reservoirs have been largely depleted or stabilized against further star formation via internal feedback mechanisms [13].

In contrast, the star-forming galaxies (open markers in Figure 9) are generally bluer. This blue color directly indicates a high fraction of young stellar populations and ongoing star formation activity. This trend persists across the full mass range, implying that RPS candidate galaxies do not simply occupy a particular stellar mass regime; rather, they represent a star-forming subset active at each mass scale. Their blue colors suggest that these systems are still actively forming stars, which may be maintained or temporarily enhanced during ram-pressure interaction as the external ICM pressure compresses the interstellar medium and triggers short-lived bursts of star formation before the eventual quenching process begins.

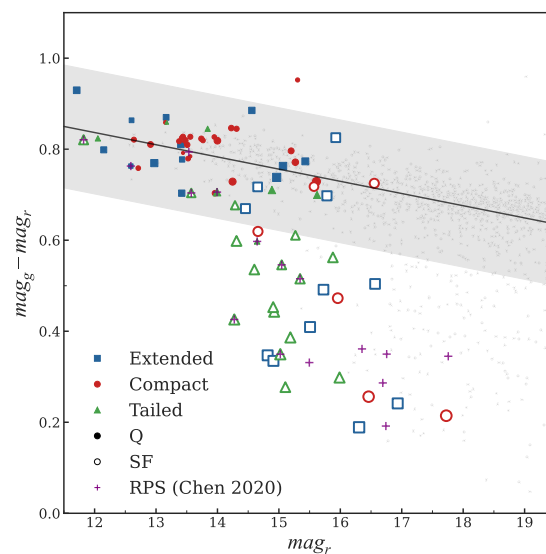


Figure 9. Color ($\text{mag}_g - \text{mag}_r$) as a function of mag_r for Coma cluster galaxies. Marker types and colors are the same as in Figure 7. The size of markers is scaled with $\log \text{sSFR}$. The black solid line is the fitted red sequence derived from the color distribution of the spectroscopic data, with the shaded grey area indicating the 3σ confidence interval of the fit.

4. Environment Influence

To evaluate the environmental influences on the radio properties of our sample, we examined the distribution of radio sources in the $R - V$ diagram (Figure 10), where R is the projected cluster-centric radius and V is the line-of-sight velocity. The diagram plots the projected cluster-centric radius normalized by R_{200} against the line-of-sight velocity offset normalized by the velocity dispersion ($\Delta V_{\text{los}}/\sigma_{\text{los}}$, where $\Delta V_{\text{los}} = |V_{\text{los}}|$). This representation provides valuable insight into the dynamical histories of galaxies within the cluster, as different regions correspond to distinct stages of infall and environmental processing (e.g., [42–44]). To quantify where infalling galaxies are located within the cluster environment, we adopt the method developed by Dou and Yu [44], which uses a set of parallel oblique lines in the $R - V$ diagram. While R_{200} serves as a global proxy for the cluster's dynamical boundary, we also incorporate R_{500} into our radial analysis. This choice is motivated by the strong correlation between R_{500} and the hot ICM properties, facilitating a more direct comparison between radio morphologies and the ICM density peak. We define the x-intercept of these lines as d_R , which serves as a relative proxy for the infall stage of the cluster member galaxies. This d_R distance is defined by $d_R = -(|V_{\text{los}}|/\sigma_{\text{los}} - kR/R_{200})/k$, where the slope $k = -3.7$ is adopted from the TNG300 simulation [44]. It can be directly compared to the normalized projected radius R/R_{200} . By construction, smaller values of d_R correspond to galaxies that have likely experienced earlier infall and are typically located closer to the cluster core, whereas larger values of d_R indicate later infall stages and are generally associated with galaxies in the cluster outskirts. In this framework, galaxies with $d_R > 1$ correspond to galaxies located beyond R_{200} and therefore trace the cluster outskirts.

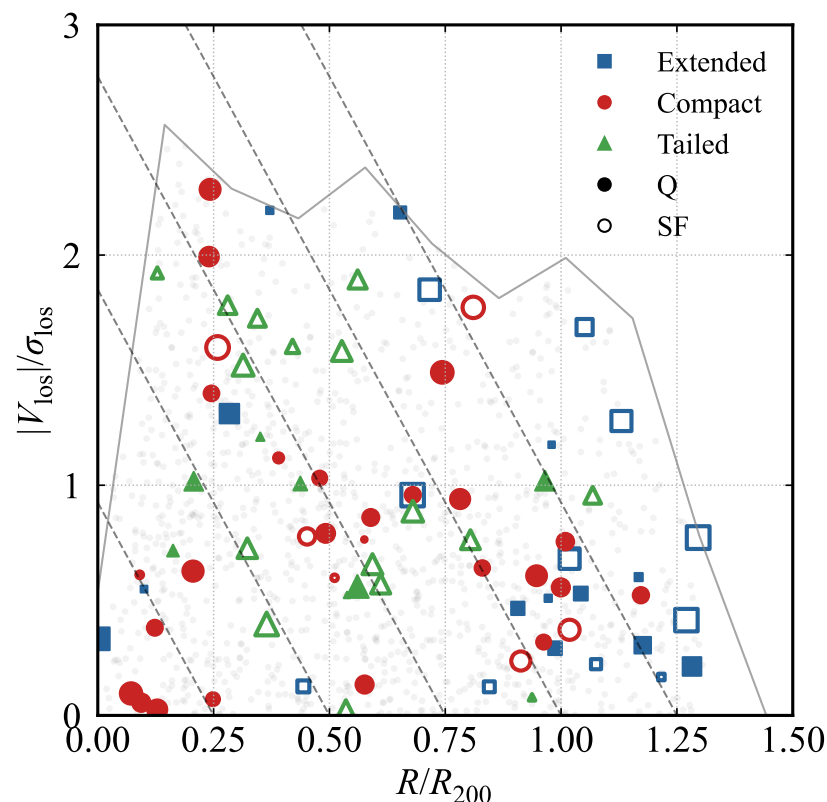


Figure 10. R - V diagram for galaxies within $1.35 R_{200}$ around the center of Coma cluster. The solid broken line shows the same caustic line as in Figure 2. The parallel dashed lines represent characteristic dynamical zones [44]. Marker types and colors are the same as in Figure 7. The size of markers is scaled with $\log L_{144}$.

From the d_R distribution histograms of these sources (Figure 11), we find that the majority (18 out of 25, $\sim 72\%$) of extended (E) radio sources are located beyond $d_R > 1.0$. These sources reside in the cluster outskirts, and their extended morphologies are consequently less likely to be disturbed by the dense cluster environment. In contrast, most (18 out of 23, $\sim 78\%$) of the tailed (T) radio sources are concentrated in the intermediate region ($0.4 < d_R < 1.0$). This distribution strongly suggests that the intense interaction between radio-emitting activity and the dense environment, which results in the characteristic swept-back morphology, primarily occurs in the cluster's main infall region. Furthermore, the compact (C) radio sources exhibit a spatial distribution peaking around $R \approx R_{500}$ ($d_R \approx 0.65$). This indicates that the dense cluster environment not only affects the morphology of radio sources but may also play a role in modulating AGN activity.

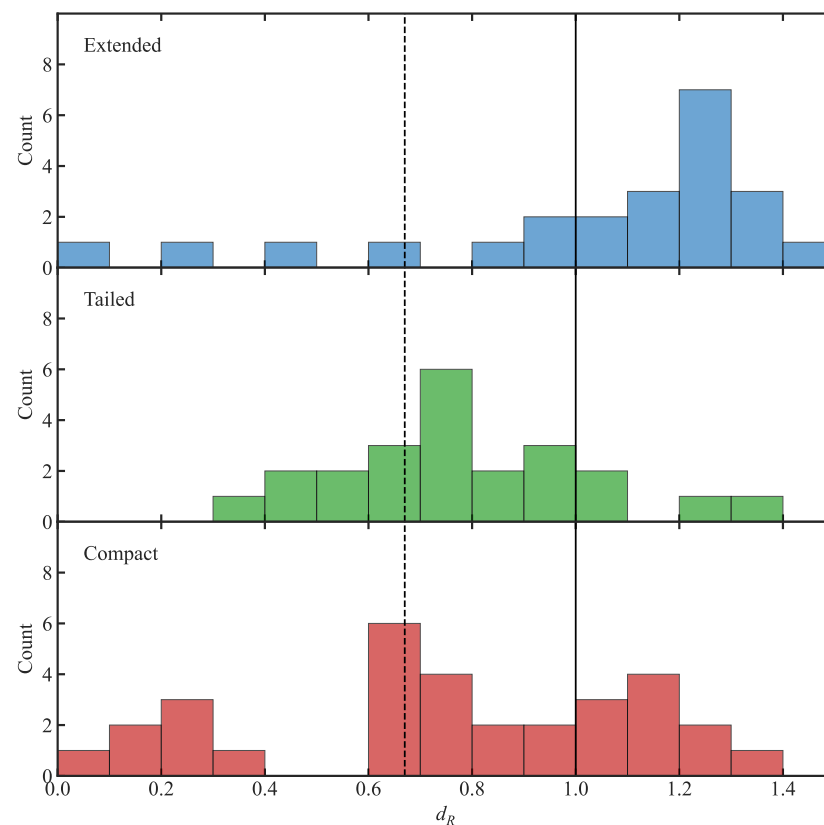


Figure 11. d_R distributions for the three radio morphology types: Extended (**top**), Tailed (**middle**), and Compact (**bottom**). In each panel, the vertical black dashed line denotes the location of R_{500} , while the vertical black solid line marks R_{200} .

We next examined the proportion of radio sources across different cluster environments. When using the projected radial distance (R/R_{200}) alone (the upper panel of Figure 12), the fraction of radio activity appears similar in SF and quiescent (Q) member galaxies, except in the very central region where SF galaxies are rare. This interpretation is further supported by HI observations of Coma galaxies. Healy et al. [45] found that HI deficiency increases significantly within $R \approx 0.5R_{200}$, while galaxies at $0.6 < R/R_{200} < 1.0$ generally remain HI-normal. Our finding of an enhanced radio fraction near R_{500} ($\sim 0.65R_{200}$) corresponds precisely to this transition zone. It suggests that as galaxies penetrate the R_{500} boundary, the rapid removal of HI reservoirs (as documented by [45]) is accompanied by a transient boost in radio emission likely driven by ram-pressure-induced gas compression before the galaxies ultimately become HI-deficient and quenched in the cluster core. However, a complicating factor is the observation that the overall radio fraction shows relatively

high proportions both around R_{200} and within R_{500} on this plot, a trend that is difficult to interpret due to projection effects.

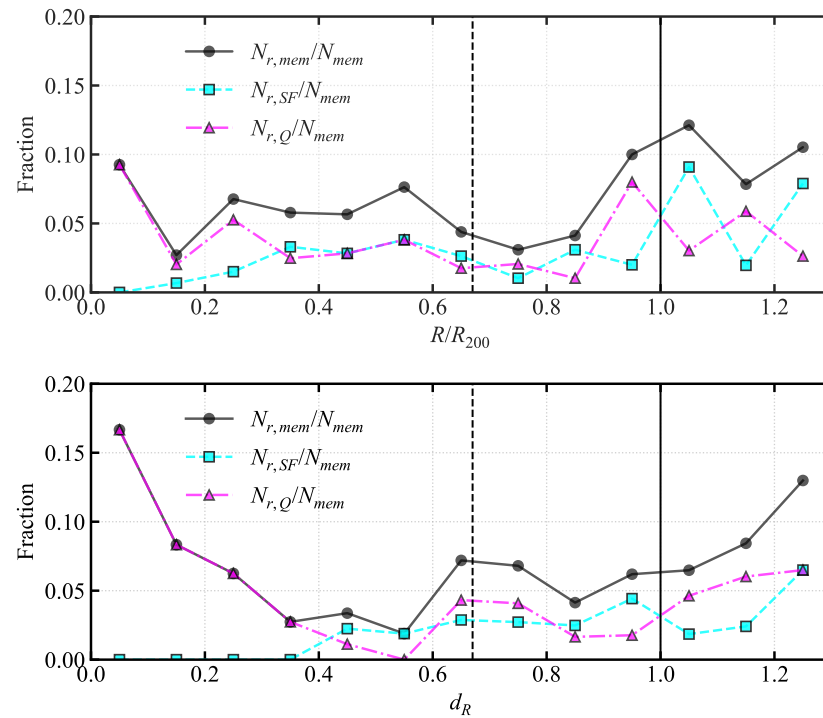


Figure 12. (Upper panel): Fraction of radio sources as a function of R/R_{200} for various populations in the Coma cluster. Black circles represent the fraction of all radio sources relative to the total optical member population. Cyan squares and magenta triangles denote the fractions of star-forming and quiescent galaxies with radio emission, respectively, both normalized to the total optical population. Vertical black dashed and solid lines indicate the positions of R_{500} and R_{200} . **(Bottom panel):** Radio source fractions as a function of the d_R . Symbol types, colors and lines are consistent with the upper panel.

By adopting the phase-space distance d_R as the x-axis (the lower panel of Figure 11), we effectively mitigate projection effects to a certain extent, and the environmental trends become clearer. The radio fraction exhibits relatively high proportions at three distinct locations in phase space: the core region ($d_R \approx 0$), an intermediate peak around $d_R \approx 0.65$ (corresponding to R_{500}), and the infall region beyond the virial radius ($d_R > 1$). At the cluster center, the enhanced radio fraction is predominantly driven by massive quiescent galaxies, implying more frequent accretion activity in the supermassive black holes within these systems.

The peak in radio activity observed around the intermediate distance (R_{500} , or $d_R \approx 0.65$) is predominantly caused by compact and tailed radio sources (as detailed in Figure 12). This peak coincides with the region where the density of the ICM increases rapidly, thereby maximizing the ram pressure experienced by infalling galaxies. This is strongly supported by the concentration of tailed sources here. Moreover, AGN accretion activity may be transiently boosted by external perturbations, possibly related to the recent merging event involving the infalling NGC 4839 group [18,46].

Conversely, the generally declining trend in the radio fraction towards the cluster center (for $d_R < 1$) and the reduced activity beyond R_{200} (where d_R is large) are also understandable. The dense cluster environment ultimately strips away the cold gas necessary for both efficient star formation and sustained AGN accretion, leading to the long-term suppression of radio activity.

5. Conclusions

In this study, we presented a systematic analysis of the radio activity within the Coma cluster by combining deep 144 MHz observations from LOFAR (LoTSS DR2) with optical spectroscopy and photometry from DESI and SDSS. We identified 79 cluster members with radio emission within $1.35R_{200}$ (1.8 deg^2) and investigated their physical properties and environmental dependence.

Our main conclusions are summarized as follows:

(1) The Number and Morphology of Radio Sources. Thanks to LOFAR's superior sensitivity, we present the most comprehensive catalog of radio members of the Coma Cluster to date. Our sample (79 members) more than doubles the population identified at 1.4 GHz by Miller et al. [19] and substantially expands upon the 24 members recently surveyed with uGMRT by Lal et al. [20]. The observed source count distribution ($\log N$ - $\log S$) shows a slight excess above the average trend, but it is not contributed by radio activity within the cluster. Our 79 radio members are classified into 31 compact sources, 25 extended sources, and 23 tailed structures. Compared with existing reports [7], the proportion of extended sources is significantly higher, while the proportion of compact sources is markedly lower, regardless of whether the system is merging or relaxing. However, the proportion of tailed sources is comparable to that of the merging system.

(2) Bimodal Nature of Radio Hosts. The radio population exhibits a clear bimodality in the star formation rate versus stellar mass plane, separating into massive quiescent galaxies and active star-forming systems. This optical state is strongly correlated with radio morphology. Compact (C) sources are predominantly hosted by massive, quiescent galaxies on the red sequence. Their radio emission exceeds the level expected from star formation alone, confirming it is dominated by central AGN activity. Tailed (T) sources are largely associated with star-forming galaxies. Their alignment with the star-forming main sequence and their specific morphologies indicate that their radio emission originates primarily from star formation activity occurring within gas stripped by ram pressure.

(3) Phase-Space Evolution. Using the phase-space distance (d_R) as a proxy for infall time, we mapped the distinct environmental histories of these populations. Extended (E) sources are preferentially located in the cluster outskirts ($d_R > 1$), where they are entering the cluster environment for the first time and remain relatively undisturbed. Tailed (T) sources are concentrated in the infall region ($0.4 < d_R < 1.0$), confirming that the transformation of galaxy morphology via ram pressure stripping is most active during the first infall into the high-density ICM.

(4) Environmental Modulation of Activity. The fractions of radio-bright galaxies are not uniform across the cluster. We observed elevated radio fractions in the core (due to massive AGN) and, notably, a secondary peak around R_{500} ($d_R \approx 0.65$). This intermediate peak, populated by both compact and tailed sources, suggests that the dense environment at R_{500} acts as a "trigger zone." Here, increasing ram pressure drives morphological disturbances (tails), while external perturbations (potentially linked to substructure mergers like NGC 4839) may transiently boost AGN accretion before the galaxies are ultimately quenched in the core.

In summary, our multi-wavelength analysis demonstrates that the Coma cluster environment plays a dual role in galaxy evolution. It initially promotes distinct radio morphologies and enhances activity during infall (at $\sim R_{500}$), before ultimately stripping the gas reservoirs required to sustain star formation and AGN activity in the cluster center.

Author Contributions: Conceptualization, X.H. and H.Y.; methodology, X.H. and H.Y.; software, X.H.; validation, X.H., H.Y. and T.P.; formal analysis, X.H.; investigation, X.H. and H.D.; resources, X.H.

and T.P.; data curation, X.H.; writing—original draft preparation, X.H.; writing—review and editing, H.Y., H.Z. and E.M.; visualization, X.H.; supervision, H.Y., H.Z. and C.L.; project administration, H.Y.; funding acquisition, H.Y., H.Z. and C.L. All authors have read and agreed to the published version of the manuscript.

Funding: This work has been supported by the National Natural Science Foundation of China No. 12573003, the National Key Research and Development Program of China (No. 2023YFC2206704), the China Manned Space Program with grant No. CMS-CSST-2025-A04 and the International Partnership Program of Chinese Academy of Sciences, Grant No. 013GJHZ2024015FN. H.Zou. acknowledges the support from the National Key R&D Program of China (grant Nos. 2023YFA1607804 and 2025YFE0202300) and the National Natural Science Foundation of China (NSFC; grant Nos. 12120101003 and 12373010) and China Manned Space Project (No. CMS-CSST-2025-A06).

Institutional Review Board Statement: Not applicable.

Informed Consent Statement: Not applicable.

Data Availability Statement: The data used in this study are from publicly available surveys. The LOFAR Two-Metre Sky Survey (LoTSS) DR2 data can be accessed via the LOFAR Surveys website at <https://lofar-surveys.org/> (accessed on 28 May 2025). The DESI Legacy Imaging Surveys (DR9) data are available at <https://www.legacysurvey.org/> (accessed on 28 November 2023). Spectroscopic data from the Dark Energy Spectroscopic Instrument (DESI) DR1 and the Sloan Digital Sky Survey (SDSS) are available through their respective archives at <https://data.desi.lbl.gov/> (accessed on 29 June 2025) and <https://www.sdss.org/> (accessed on 29 June 2025).

Acknowledgments: The authors thank the referees for their corrections and valuable suggestions to improve the paper.

Conflicts of Interest: The authors declare no conflicts of interest.

Appendix A. Physical Parameters of Host Galaxies of Radio Sources in the Coma Cluster

In this appendix, we present the properties of the 79 radio-detected galaxies within the Coma cluster. Table A1 lists the coordinates, spectroscopic measurements from DESI, and radio properties from LOFAR.

Table A1. Physical Parameters of Host Galaxies of Radio Sources in the Coma Cluster

ID	RA	Dec	z	logSFR	logM _*	logL ₁₄₄	g-r	SNR	A	M _{type}	Name
1	193.2233	28.3713	0.0236	-1.0157	11.1675	23.2975	0.8106	159.4	Q	E	
2	193.2814	28.2412	0.0235	-0.6578	8.6951	21.3763	0.2414	4.2	SF	E	
3	193.6383	27.6328	0.0244	-1.5908	10.7169	21.8449	0.8852	10.0	Q	E	
4	193.7237	28.4170	0.0247	-1.2597	10.5773	21.6050	0.7287	7.8	Q	P	
5	193.7535	27.4834	0.0232	-0.5168	9.6409	20.9695	0.6976	6.6	SF	T	
6	193.9491	28.2562	0.0271	-2.7578	10.6619	21.7663	0.9521	15.9	Q	P	
7	194.0457	28.1632	0.0290	-1.4242	10.5203	22.3104	0.7733	32.7	Q	E	
8	194.1160	26.9874	0.0215	-2.0609	11.1503	21.3991	0.7584	7.1	Q	P	NGC 4819
9	194.1191	27.2913	0.0251	0.3423	10.0223	22.3951	0.5356	12.6	SF	T	IC 3913
10	194.2690	27.7730	0.0252	-1.0280	10.0424	21.4552	0.7290	8.3	Q	P	
11	194.2975	29.0450	0.0251	-2.6986	11.0690	21.3544	0.7843	13.1	Q	P	
12	194.3515	27.4978	0.0245	-1.3934	11.4962	23.9337	0.8238	225.1	Q	T	NGC 4839
13	194.3832	28.4770	0.0226	-1.8004	11.2456	21.3970	0.8209	7.7	Q	P	NGC 4841
14	194.3868	27.6103	0.0202	-2.2230	10.8419	21.1927	0.8175	16.1	Q	P	NGC 4840
15	194.3911	28.4822	0.0209	-2.4123	10.7735	20.8330	0.7794	5.1	Q	P	NGC 4841B
16	194.3994	27.4932	0.0244	-2.0729	10.8500	21.8726	0.8449	23.0	Q	T	NGC 4842A
17	194.4861	27.0375	0.0247	-2.2138	10.3507	21.2190	0.7963	6.8	Q	P	
18	194.4908	28.0615	0.0272	-0.2679	10.0576	22.7905	0.5459	73.1	SF	T	KUG 1255+283
19	194.5234	28.2425	0.0241	0.1863	10.8921	23.1299	0.7039	229.3	SF	T	NGC 4848
20	194.5295	26.7871	0.0240	-0.6892	9.5043	21.4055	0.7250	4.8	SF	P	
21	194.5386	28.7086	0.0254	-0.2710	10.5953	22.7259	0.6768	37.9	SF	T	
22	194.5776	27.3108	0.0248	0.1650	9.8159	22.6033	0.5623	59.4	SF	T	2MASX J12581865+2718387
23	194.6064	28.1289	0.0274	-0.1316	9.4701	21.5277	0.4726	12.5	SF	P	
24	194.6230	28.3012	0.0197	-2.0608	9.7707	21.9931	0.6995	38.5	Q	T	
25	194.6473	27.2647	0.0246	0.3400	9.5105	22.4461	0.3864	46.9	SF	T	Mrk 56
26	194.6553	27.1765	0.0256	0.4868	9.7762	22.5896	0.4429	39.6	SF	E	Mrk 57
27	194.6577	27.4639	0.0209	-0.7475	9.8283	21.2547	0.7178	6.0	SF	P	

Table A1. Cont.

ID	RA	Dec	z	logSFR	logM _*	logL ₁₄₄	g-r	SNR	A	M _{type}	Name
28	194.6601	27.5441	0.0199	-2.2441	9.9729	20.9931	0.7714	10.2	Q	P	
29	194.6661	26.7594	0.0249	-0.2461	9.0988	22.2670	0.3091	9.4	SF	E	
30	194.6910	28.5430	0.0214	-0.6492	8.0268	21.0120	0.2144	5.2	SF	P	
31	194.7333	27.8334	0.0250	-0.6321	10.8093	22.3000	0.7057	34.9	Q	T	IC 3949
32	194.7576	28.2253	0.0268	-2.3230	10.9372	21.2362	0.8268	10.3	Q	P	
33	194.7576	26.8157	0.0239	-2.4211	11.1191	21.1945	0.8588	7.1	Q	P	NGC 4859
34	194.7721	27.6443	0.0181	0.4105	9.6307	22.1972	0.4258	69.3	SF	T	Mrk 58
35	194.7831	27.8550	0.0220	-2.1787	10.5967	21.2490	0.8464	6.7	Q	P	IC 3960
36	194.8047	27.9770	0.0227	-1.7094	10.8568	21.7360	0.8194	10.6	Q	P	NGC 4864
37	194.8195	27.1061	0.0280	-0.3123	10.1353	22.3609	0.8254	58.6	SF	E	
38	194.8464	28.4886	0.0233	-0.1814	9.5231	21.6367	0.4914	10.3	SF	E	
39	194.8725	27.8501	0.0228	-2.3703	10.5905	21.4116	0.8449	8.0	Q	P	IC 3976
40	194.9130	28.8955	0.0204	-2.5466	10.9182	21.5458	0.8250	29.6	Q	P	IC 3990
41	194.9173	28.6308	0.0178	-0.2191	9.3282	22.2849	0.2772	7.7	SF	T	2MASX J12594009+2837507
42	195.0185	27.9876	0.0213	-3.0756	10.7331	20.8999	0.7918	5.2	Q	P	NGC 4886
43	195.0381	27.8664	0.0178	-0.3794	9.5411	21.3453	0.5153	25.4	SF	T	
44	195.0737	27.9553	0.0231	-1.9421	10.8803	21.5432	0.8097	17.5	Q	P	NGC 4898A
45	195.0747	28.2024	0.0284	-1.3262	11.2895	21.5054	0.8103	14.5	Q	P	NGC 4895
46	195.1303	28.9505	0.0233	-0.4629	9.1845	21.5757	0.5040	4.5	SF	E	
47	195.1398	27.5041	0.0186	-0.3401	8.8462	21.5959	0.2983	11.1	SF	T	
48	195.1404	27.6377	0.0250	0.4759	9.4902	22.5324	0.3495	51.8	SF	E	KUG 1258+279A
49	195.1580	28.0575	0.0258	-2.2341	10.5447	23.2354	0.5974	203.6	Q	T	IC 4040
50	195.1649	29.0193	0.0243	-1.4084	10.9222	22.4582	0.7034	5.4	Q	E	IC 842
51	195.1782	27.9713	0.0213	-2.1353	10.7590	21.6363	0.8231	12.3	Q	P	IC 4042
52	195.2027	28.0907	0.0232	-2.3876	10.8586	21.1329	0.8192	5.3	Q	P	IC 4045
53	195.2335	27.7908	0.0266	-1.9604	11.3670	23.4662	0.7630	72.3	Q	E	NGC 4911
54	195.3530	29.3097	0.0238	-0.7136	11.0558	22.9374	0.7694	343.4	Q	E	
55	195.3589	27.8860	0.0183	-0.5649	9.5893	22.0810	0.8207	8.1	SF	T	NGC 4921
56	195.3900	29.1306	0.0244	-1.5341	11.1295	22.5343	0.8700	87.4	Q	E	IC 843
57	195.4307	29.0446	0.0238	-1.8624	11.0517	22.5015	0.7774	22.9	Q	E	IC 4088
58	195.4899	28.0058	0.0258	-2.4214	11.2327	22.5212	0.8588	75.4	Q	T	NGC 4927
59	195.5175	29.2534	0.0244	-2.0235	10.9985	21.2754	0.8273	12.4	Q	P	
60	195.5328	27.6483	0.0231	0.6086	10.1078	22.4365	0.5984	43.9	SF	T	NGC 4926A
61	195.5361	28.3871	0.0253	-1.3320	10.7821	21.3179	0.8186	10.4	Q	P	
62	195.5534	28.2148	0.0273	0.4652	9.9039	22.5737	0.4530	38.7	SF	T	
63	195.6069	28.8581	0.0224	-0.2017	8.6330	21.3629	0.2562	9.0	SF	P	
64	195.8177	28.0303	0.0204	-2.0619	10.7009	21.2667	0.7033	10.7	Q	P	NGC 4934
65	196.1489	28.6277	0.0224	-0.0207	9.3745	21.5319	0.4092	12.6	SF	E	
66	196.4729	28.1124	0.0246	-1.2821	10.3171	21.9081	0.7629	18.3	Q	E	
67	196.6517	27.8729	0.0209	-0.1819	10.3712	22.6134	0.7172	99.0	SF	E	
68	195.0339	27.9769	0.0215	-0.6327	11.4979	21.8058	0.9295	46.6	Q	E	NGC 4889
69	194.3800	26.5122	0.0241	0.0311	10.3631	22.5834	0.6695	57.3	SF	E	IC 837
70	194.6664	26.7595	0.0249	-0.1239	8.9040	22.2666	0.1889	9.4	SF	E	
71	194.8988	27.9593	0.0239	-1.0247	11.4851	24.1498	0.7986	707.3	Q	E	NGC 4874
72	193.4747	28.1867	0.0256	-0.4953	10.0399	22.0574	0.6107	6.8	SF	T	
73	193.7299	27.4127	0.0262	-1.7811	11.3985	21.7893	0.8635	12.0	Q	E	NGC 4798
74	194.6801	28.9101	0.0278	0.0657	10.2042	21.4637	0.6192	5.1	SF	P	
75	195.1487	27.5742	0.0170	-0.9065	10.1042	21.8469	0.7380	38.2	Q	E	
76	195.2148	28.0429	0.0292	-1.8349	11.1536	21.6187	0.8274	16.0	Q	P	NGC 4908
77	196.0768	28.4681	0.0258	-1.3036	10.2698	23.4086	0.7104	358.6	Q	T	
78	196.0945	28.8108	0.0265	0.3497	9.7524	22.3147	0.3471	18.3	SF	E	
79	196.1106	27.3044	0.0184	-0.0358	9.3695	21.9423	0.3349	10.6	SF	E	

Notes . Column (1): Radio source ID. Column (2)–(3): Right Ascension and Declination (J2000) in decimal degrees. Column (4): Spectroscopic redshift from the DESI survey. Column (5): Logarithm of the star formation rate in units of $M_{\odot} \text{ yr}^{-1}$. Column (6): Logarithm of the stellar mass in units of M_{\odot} . Column (7): Logarithm of the radio luminosity at 144 MHz in units of W Hz^{-1} . Column (8): Optical color ($g - r$) corrected for Galactic extinction. Column (9): Peak signal-to-noise ratio (SNR) of the LOFAR radio emission. Column (10): Star-forming activity: star-forming (SF) or quiescent (Q). Column (11): Radio morphology: C (Compact), E (Extended), or T (Tailed). Column (12): Galaxy name, when available.

Appendix B. Galaxies with Large Radio-Optical Offsets

In this section, we present the multi-wavelength images for cluster members exhibiting a significant positional offset ($6''$) between their radio emission centroid and optical center. Such offsets are often indicative of environmental processing, where the relativistic plasma is displaced from the stellar disk due to the ram pressure of the intracluster medium (ICM).

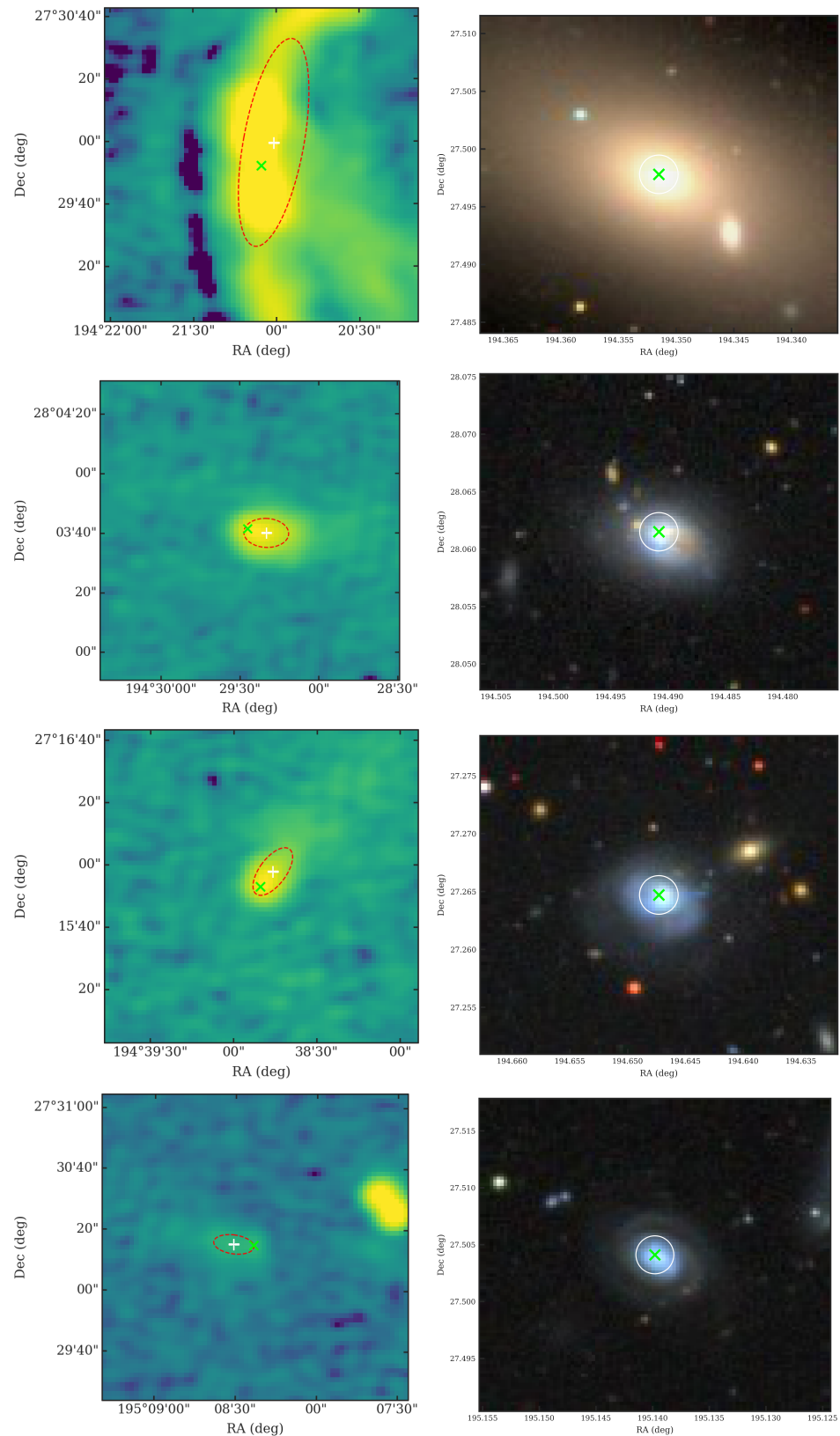


Figure A1. Radio and optical postage stamps for the sub-sample of Coma cluster members with a radio-optical offset exceeding $6''$. The left panels display LOFAR 144 MHz radio continuum images ($100'' \times 100''$), while the right panels show the corresponding optical images from DESI. In all panels, green “x” symbols indicate the optical galactic centers, and white crosses denote the centroids of the radio emission. The red dashed ellipses in the radio images represent the morphology detections of the radio emission. The white circles in the optical images have a radius of $6''$. The sub-sample includes: ID 12 (offset = $8.41''$), ID 18 ($6.26''$), ID 25 ($6.24''$), and ID 47 ($6.59''$).

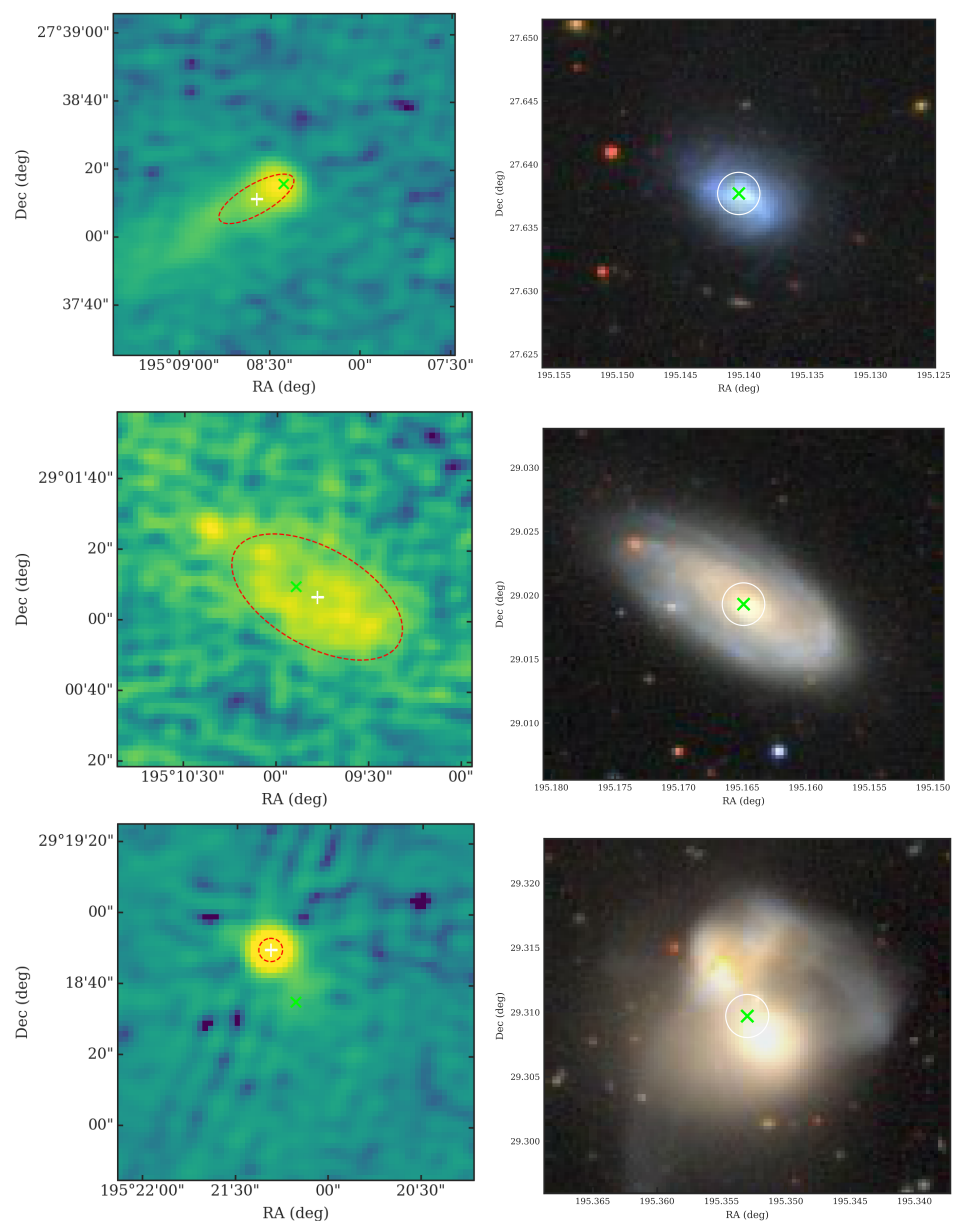


Figure A2. Radio and optical postage stamps for the sub-sample of Coma cluster members with a radio-optical offset exceeding $6''$ (Continued). The sub-sample includes: ID 48 (offset = $9.29''$), ID 50 ($6.55''$), and ID 54 ($16.28''$).

References

1. Gunn, J.E.; Gott, J.R. III. On the Infall of Matter Into Clusters of Galaxies and Some Effects on Their Evolution. *Astrophys. J.* **1972**, *176*, 1. <https://doi.org/10.1086/151605>.
2. Boselli, A.; Gavazzi, G. Environmental Effects on Late-Type Galaxies in Nearby Clusters. *Publ. Astron. Soc. Pac.* **2006**, *118*, 517–559. <https://doi.org/10.1086/500691>.
3. Bregman, J.N. Continuum radiation from active galactic nuclei. *Astron. Astrophys. Rev.* **1990**, *2*, 125–166. <https://doi.org/10.1007/BF00872765>.
4. Turner, J.L.; Ho, P.T.P. Bright Radio Continuum Emission from Star Formation in the Cores of Nearby Spiral Galaxies. *Astrophys. J.* **1994**, *421*, 122. <https://doi.org/10.1086/173631>.
5. Klein, U.; Lisenfeld, U.; Verley, S. Radio synchrotron spectra of star-forming galaxies. *Astron. Astrophys.* **2018**, *611*, A55. <https://doi.org/10.1051/0004-6361/201731673>.
6. Panessa, F.; Baldi, R.D.; Laor, A.; Padovani, P.; Behar, E.; McHardy, I. The origin of radio emission from radio-quiet active galactic nuclei. *Nat. Astron.* **2019**, *3*, 387–396. <https://doi.org/10.1038/s41550-019-0765-4>.

7. Rickel, M.; Moravec, E.; Gordon, Y.A.; Hardcastle, M.J.; Pierce, J.C.S.; Bilton, L.E.; Roberts, I.D. The Merging Galaxy Cluster Environment Affects the Morphology of Radio Active Galactic Nuclei. *Astrophys. J.* **2025**, *983*, 138. <https://doi.org/10.3847/1538-4357/adbb5e>.
8. Ledlow, M.J.; Owen, F.N. 20 CM VLA Survey of Abell Clusters of Galaxies. VI. Radio/Optical Luminosity Functions. *Astron. J.* **1996**, *112*, 9. <https://doi.org/10.1086/117985>.
9. Wing, J.D.; Blanton, E.L. Galaxy Cluster Environments of Radio Sources. *Astron. J.* **2011**, *141*, 88. <https://doi.org/10.1088/0004-6256/141/3/88>.
10. van Weeren, R.J.; de Gasperin, F.; Akamatsu, H.; Brügger, M.; Feretti, L.; Kang, H.; Stroe, A.; Zandanel, F. Diffuse Radio Emission from Galaxy Clusters. *Space Sci. Rev.* **2019**, *215*, 16. <https://doi.org/10.1007/s11214-019-0584-z>.
11. Salim, S.; Rich, R.M. Star Formation Signatures in Optically Quiescent Early-type Galaxies. *Astrophys. J. Lett.* **2010**, *714*, L290–L294. <https://doi.org/10.1088/2041-8205/714/2/L290>.
12. Capetti, A.; Brienza, M.; Balmaverde, B.; Best, P.N.; Baldi, R.D.; Drabent, A.; Gürkan, G.; Röttgering, H.J.A.; Tasse, C.; Webster, B. The LOFAR view of giant, early-type galaxies: Radio emission from active nuclei and star formation. *Astron. Astrophys.* **2022**, *660*, A93. <https://doi.org/10.1051/0004-6361/202142911>.
13. Best, P.N. The environmental dependence of radio-loud AGN activity and star formation in the 2dFGRS. *Mon. Not. R. Astron. Soc.* **2004**, *351*, 70–82. <https://doi.org/10.1111/j.1365-2966.2004.07752.x>.
14. Comerford, J.M.; Negus, J.; Müller-Sánchez, F.; Eracleous, M.; Wylezalek, D.; Storchi-Bergmann, T.; Greene, J.E.; Barrows, R.S.; Nevin, R.; Roy, N.; et al. A Catalog of 406 AGNs in MaNGA: A Connection between Radio-mode AGNs and Star Formation Quenching. *Astrophys. J.* **2020**, *901*, 159. <https://doi.org/10.3847/1538-4357/abb2ae>.
15. Churazov, E.; Khabibullin, I.; Bykov, A.M.; Lyskova, N.; Sunyaev, R. Tempestuous life beyond R_{500} : X-ray view on the Coma cluster with SRG/eROSITA. II. Shock and relic. *Astron. Astrophys.* **2023**, *670*, A156. <https://doi.org/10.1051/0004-6361/202244021>.
16. Dey, A.; Schlegel, D.J.; Lang, D.; Blum, R.; Burleigh, K.; Fan, X.; Findlay, J.R.; Finkbeiner, D.; Herrera, D.; Juneau, S.; et al. Overview of the DESI Legacy Imaging Surveys. *Astron. J.* **2019**, *157*, 168. <https://doi.org/10.3847/1538-3881/ab089d>.
17. DESI Collaboration.; Abdul-Karim, M.; Adame, A.G.; Aguado, D.; Aguilar, J.; Ahlen, S.; Alam, S.; Aldering, G.; Alexander, D.M.; Alfarsy, R.; et al. Data Release 1 of the Dark Energy Spectroscopic Instrument. *arXiv e-prints* **2025**, p. arXiv:2503.14745. <https://doi.org/10.48550/arXiv.2503.14745>.
18. Churazov, E.; Khabibullin, I.; Lyskova, N.; Sunyaev, R.; Bykov, A.M. Tempestuous life beyond R_{500} : X-ray view on the Coma cluster with SRG/eROSITA. I. X-ray morphology, recent merger, and radio halo connection. *Astron. Astrophys.* **2021**, *651*, A41. <https://doi.org/10.1051/0004-6361/202040197>.
19. Miller, N.A.; Hornschemeier, A.E.; Mobasher, B. A Deep Very Large Array Radio Continuum Survey of the Core and Outskirts of the Coma Cluster. *Astron. J.* **2009**, *137*, 4436–4449. <https://doi.org/10.1088/0004-6256/137/5/4436>.
20. Lal, D.V.; Lyskova, N.; Zhang, C.; Venturi, T.; Forman, W.R.; Jones, C.; Churazov, E.M.; van Weeren, R.J.; Bonafede, A.; Miller, N.A.; et al. High-resolution, High-sensitivity, Low-frequency uGMRT View of Coma Cluster of Galaxies. *Astrophys. J.* **2022**, *934*, 170. <https://doi.org/10.3847/1538-4357/ac7a9b>.
21. Shimwell, T.W.; Röttgering, H.J.A.; Best, P.N.; Williams, W.L.; Dijkema, T.J.; de Gasperin, F.; Hardcastle, M.J.; Heald, G.H.; Hoang, D.N.; Horneffer, A.; et al. The LOFAR Two-metre Sky Survey. I. Survey description and preliminary data release. *Astron. Astrophys.* **2017**, *598*, A104. <https://doi.org/10.1051/0004-6361/201629313>.
22. Shimwell, T.W.; Hardcastle, M.J.; Tasse, C.; Best, P.N.; Röttgering, H.J.A.; Williams, W.L.; Botteon, A.; Drabent, A.; Mechev, A.; Shulevski, A.; et al. The LOFAR Two-metre Sky Survey. V. Second data release. *Astron. Astrophys.* **2022**, *659*, A1. <https://doi.org/10.1051/0004-6361/202142484>.
23. Almeida, A.; Anderson, S.F.; Argudo-Fernández, M.; Badenes, C.; Barger, K.; Barrera-Ballesteros, J.K.; Bender, C.F.; Benitez, E.; Besser, F.; Bird, J.C.; et al. The Eighteenth Data Release of the Sloan Digital Sky Surveys: Targeting and First Spectra from SDSS-V. *Astrophys. J. Suppl. Ser.* **2023**, *267*, 44. <https://doi.org/10.3847/1538-4365/acda98>.
24. Hahn, C.; Wilson, M.J.; Ruiz-Macias, O.; Cole, S.; Weinberg, D.H.; Moustakas, J.; Kremin, A.; Tinker, J.L.; Smith, A.; Wechsler, R.H.; et al. The DESI Bright Galaxy Survey: Final Target Selection, Design, and Validation. *Astron. J.* **2023**, *165*, 253. <https://doi.org/10.3847/1538-3881/acff8>.
25. Serra, A.L.; Diaferio, A.; Murante, G.; Borgani, S. Measuring the escape velocity and mass profiles of galaxy clusters beyond their virial radius. *Mon. Not. R. Astron. Soc.* **2011**, *412*, 800–816. <https://doi.org/10.1111/j.1365-2966.2010.17946.x>.
26. Serra, A.L.; Diaferio, A. Identification of Members in the Central and Outer Regions of Galaxy Clusters. *Astrophys. J.* **2013**, *768*, 116. <https://doi.org/10.1088/0004-637X/768/2/116>.
27. Zou, H.; Sui, J.; Saintonge, A.; Scholte, D.; Moustakas, J.; Siudek, M.; Dey, A.; Juneau, S.; Guo, W.; Canning, R.; et al. A Large Sample of Extremely Metal-poor Galaxies at $z < 1$ Identified from the DESI Early Data. *Astrophys. J.* **2024**, *961*, 173. <https://doi.org/10.3847/1538-4357/ad1409>.
28. Boquien, M.; Burgarella, D.; Roehly, Y.; Buat, V.; Ciesla, L.; Corre, D.; Inoue, A.K.; Salas, H. CIGALE: A python Code Investigating GALaxy Emission. *Astron. Astrophys.* **2019**, *622*, A103. <https://doi.org/10.1051/0004-6361/201834156>.

29. Bonato, M.; Negrello, M.; Mancuso, C.; De Zotti, G.; Ciliegi, P.; Cai, Z.Y.; Lapi, A.; Massardi, M.; Bonaldi, A.; Sajina, A.; et al. Does the evolution of the radio luminosity function of star-forming galaxies match that of the star formation rate function? *Mon. Not. R. Astron. Soc.* **2017**, *469*, 1912–1923. <https://doi.org/10.1093/mnras/stx974>.
30. Galluzzi, V.; Behiri, M.; Giulietti, M.; Lapi, A. An Updated Repository of Sub-mJy Extragalactic Source-Count Measurements in the Radio Domain. *Galaxies* **2025**, *13*, 34. <https://doi.org/10.3390/galaxies13020034>.
31. Dow, K.L.; White, S.D.M. ROSAT Observations of Coma Cluster Galaxies. *Astrophys. J.* **1995**, *439*, 113. <https://doi.org/10.1086/175156>.
32. Wetzel, A.R.; Tinker, J.L.; Conroy, C. Galaxy evolution in groups and clusters: Star formation rates, red sequence fractions and the persistent bimodality. *Mon. Not. R. Astron. Soc.* **2012**, *424*, 232–243. <https://doi.org/10.1111/j.1365-2966.2012.21188.x>.
33. Fabian, A.C. Observational Evidence of Active Galactic Nuclei Feedback. *Annu. Rev. Astron. Astrophys.* **2012**, *50*, 455–489. <https://doi.org/10.1146/annurev-astro-081811-125521>.
34. Tadhunter, C. Radio AGN in the local universe: Unification, triggering and evolution. *Astron. Astrophys. Rev.* **2016**, *24*, 10. <https://doi.org/10.1007/s00159-016-0094-x>.
35. Chen, H.; Sun, M.; Yagi, M.; Bravo-Alfaro, H.; Brinks, E.; Kenney, J.; Combes, F.; Sivanandam, S.; Jachym, P.; Fossati, M.; et al. The ram pressure stripped radio tails of galaxies in the Coma cluster. *Mon. Not. R. Astron. Soc.* **2020**, *496*, 4654–4673. <https://doi.org/10.1093/mnras/staa1868>.
36. Igo, Z.; Merloni, A.; Hoang, D.; Buchner, J.; Liu, T.; Salvato, M.; Arcodia, R.; Bellstedt, S.; Brüggem, M.; Croston, J.H.; et al. The LOFAR - eFEDS survey: The incidence of radio and X-ray AGN and the disk-jet connection. *Astron. Astrophys.* **2024**, *686*, A43. <https://doi.org/10.1051/0004-6361/202349069>.
37. Condon, J.J. Radio emission from normal galaxies. *Annu. Rev. Astron. Astrophys.* **1992**, *30*, 575–611. <https://doi.org/10.1146/annurev.aa.30.090192.003043>.
38. Gürkan, G.; Hardcastle, M.J.; Smith, D.J.B.; Best, P.N.; Bourne, N.; Calistro-Rivera, G.; Heald, G.; Jarvis, M.J.; Prandoni, I.; Röttgering, H.J.A.; et al. LOFAR/H-ATLAS: The low-frequency radio luminosity-star formation rate relation. *Mon. Not. R. Astron. Soc.* **2018**, *475*, 3010–3028. <https://doi.org/10.1093/mnras/sty016>.
39. Best, P.N.; Kondapally, R.; Williams, W.L.; Cochrane, R.K.; Duncan, K.J.; Hale, C.L.; Haskell, P.; Małek, K.; McCheyne, I.; Smith, D.J.B.; et al. The LOFAR Two-metre Sky Survey: Deep Fields data release 1. V. Survey description, source classifications, and host galaxy properties. *Mon. Not. R. Astron. Soc.* **2023**, *523*, 1729–1755. <https://doi.org/10.1093/mnras/stad1308>.
40. Gladders, M.D.; Yee, H.K.C. A New Method For Galaxy Cluster Detection. I. The Algorithm. *Astron. J.* **2000**, *120*, 2148–2162. <https://doi.org/10.1086/301557>.
41. Sciaratta, M.; Chiosi, C.; D’Onofrio, M.; Cariddi, S. Cosmological Interpretation of the Color-Magnitude Diagrams of Galaxy Clusters. *Astrophys. J.* **2019**, *870*, 70. <https://doi.org/10.3847/1538-4357/aaf00d>.
42. Rhee, J.; Smith, R.; Choi, H.; Yi, S.K.; Jaffé, Y.; Candlish, G.; Sánchez-Jánssen, R. Phase-space Analysis in the Group and Cluster Environment: Time Since Infall and Tidal Mass Loss. *Astrophys. J.* **2017**, *843*, 128. <https://doi.org/10.3847/1538-4357/aa6d6c>.
43. Pasquali, A.; Smith, R.; Gallazzi, A.; De Lucia, G.; Zibetti, S.; Hirschmann, M.; Yi, S.K. Physical properties of SDSS satellite galaxies in projected phase space. *Mon. Not. R. Astron. Soc.* **2019**, *484*, 1702–1723. <https://doi.org/10.1093/mnras/sty3530>.
44. Dou, H.; Yu, H. Estimating infall times of galaxies around clusters: Working to achieve accurate results based on observational data. *Astron. Astrophys.* **2025**, *699*, A95. <https://doi.org/10.1051/0004-6361/202555240>.
45. Healy, J.; Blyth, S.L.; Verheijen, M.A.W.; Hess, K.M.; Serra, P.; van der Hulst, J.M.; Jarrett, T.H.; Yim, K.; Józsa, G.I.G. HI content in Coma cluster substructure. *Astron. Astrophys.* **2021**, *650*, A76. <https://doi.org/10.1051/0004-6361/202038738>.
46. Lyskova, N.; Churazov, E.; Zhang, C.; Forman, W.; Jones, C.; Dolag, K.; Roediger, E.; Sheardown, A. Close-up view of an ongoing merger between the NGC 4839 group and the Coma cluster—A post-merger scenario. *Mon. Not. R. Astron. Soc.* **2019**, *485*, 2922–2934. <https://doi.org/10.1093/mnras/stz597>.

Disclaimer/Publisher’s Note: The statements, opinions and data contained in all publications are solely those of the individual author(s) and contributor(s) and not of MDPI and/or the editor(s). MDPI and/or the editor(s) disclaim responsibility for any injury to people or property resulting from any ideas, methods, instructions or products referred to in the content.